# UC Santa Barbara
## UC Santa Barbara Previously Published Works

**Title**

Microstructure Evolution of Biphasic TiNi1+x Sn Thermoelectric Materials

**Permalink**

https://escholarship.org/uc/item/8w5861rg

**Journal**

Metallurgical and Materials Transactions A, 47(8)

**ISSN**

1073-5623 1543-1940

**Authors**

Verma, Nisha
Douglas, Jason E
Krämer, Stephan
et al.

**Publication Date**

2016-05-10

**DOI**

10.1007/s11661-016-3549-9

Peer reviewed

# Microstructure Evolution of Biphasic TiNi$_{1+x}$Sn Thermoelectric Materials

Nisha Verma, Jason E. Douglas, Stephan Krämer,
Tresa M. Pollock, Ram Seshadri, and Carlos G. Levi

Materials Department and Materials Research Laboratory
University of California, Santa Barbara, Santa Barbara, CA 93106-5050, USA

## Abstract

The effects of thermal treatment on the microstructure of bi-phasic materials comprising half-Heusler (hH) and full-Heusler (fH) phases, as well as on their associated thermal conductivity, are discussed. The focus is on a biphasic hH/fH alloy of nominal stoichiometry TiNi$_{1.2}$Sn, synthesized by containerless (magnetic levitation) induction melting. The alloy samples were exposed to various heat treatments to generate microstructures containing second phase precipitates ranging from ~10 nm to a few micrometers. The materials were characterized with regard to morphology, size, shape and orientation relationship of the fH and hH phases, both of which are present as precipitates within larger regions of the counterpart phase. The solidification path of the alloy and its implications for the subsequent microstructure evolution during heat treatment were elucidated, and relationships with the ensuing thermal conductivity were characterized.

*Submitted to ??? (December 2015)*

## Introduction

Materials enabling solid-state conversion of thermal energy into electric energy have been the subject of extensive interest in recent years [1, 2]. Thermoelectrics provide a technology for harvesting waste heat from transportation, industrial, and domestic sectors, [3-6] potentially reducing energy consumption and concomitant $CO_2$ emissions. The success and broader applicability of this technology is critically dependent on the design and synthesis of thermoelectric materials with higher efficiency.

Intermetallic half-Heusler (hH) alloys of the type $M$NiSn ($M$ = Ti, Zr, Hf) have received much attention in the recent past owing to their potential for thermoelectric power generation at higher temperature ($700 \leq T \leq 1000$K) [7-10]. These alloys with 18-valence electrons are narrow band gap semiconductors that tend to exhibit relatively high Seebeck coefficients, $S$, as well as relatively high electrical conductivity, $\sigma$. They are also appealing because they comprise elements that are inexpensive, abundant, and environment friendly. In spite of their larger power factors, $S^2\sigma$, the thermoelectric figures of merit for these materials, $ZT = S^2\sigma T/\kappa$ are usually limited to values of ~1 because of their higher thermal conductivity, $\kappa$, compared with other classes of thermoelectrics.

It is well known that microstructural features and defects can strongly influence thermoelectric properties. In consequence, many strategies have been explored for reducing $\kappa$ while preserving the power factor, mainly focused on introducing phonon scattering centers, either by (i) partial substitution of Zr/Hf for Ti and Pd/Pt for Ni [11-13], (ii) adding solutes in the nominally vacant interstitial sites of the hH structure [13] or (iii) nanostructuring through grain size refinement or incorporation of ultrafine second phases [7, 14]. Reductions in thermal conductivity while retaining the power factor have been reported for off-stoichiometric TiNiSn alloys [15], a behavior that is attributed to random occupancy of the structural vacancies in the hH structure by excess Ni atoms [16], acting as phonon scattering centers. A simultaneous increase of S and $\sigma$, which usually vary in opposite directions, has been reported at high temperature through the incorporation of nanoscale (<10 nm) coherent precipitates of full-Heusler (fH) phase, $M$Ni$_2$Sn, in a hH matrix [17]. The thermoelectric properties of these biphasic alloys are known to depend on multiple factors but the structure-property relationships are still poorly understood. Important factors affecting the transport of charge and heat carriers through a material include, but may not be limited to: (i) the degree of coherency of the interface between the matrix and the dispersed phase [18, 19]; (ii) the shape, size, distribution and volume fraction of the second phase; and (iii) an energy filtering effect at certain semiconducting/metal interfaces [20].

The present investigation aims to provide insight into the influence of heat treatment on the microstructure of a biphasic hH/fH alloy, namely TiNi$_{1.2}$Sn, and its relationship with the thermoelectric response. The composition and heat treatments were designed to yield bi-phasic composites with coherent boundaries, which could act as phonon scattering centers while leaving electrical conductivity relatively unaffected. Therefore, the paper focuses on understanding the effects of the thermal history on precipitate shape, size and orientation relationship, and their impact on thermal conductivity.

**Experimental Details**

The Ti-Ni-Sn alloys investigated were synthesized by induction levitation melting followed by annealing according to a procedure established in an earlier publication [21]. Briefly, the heat treatments involve two cycles, depicted in Figure 1. An initial exposure consisted of 24 h at 1173K, followed by 192 h at 1123K and cooling in air. The sample was then exposed to a second heat treatment of 5 h at 1423K, close to the solidus temperature of TiNiSn (hH), followed by cooling at either ~1 K/min (HT-SC) or an air "quench" (HT-Q).

The constituent phases were first identified by X-ray diffraction (XRD) using an X'Pert X-ray diffractometer (PANalytical). The molar fractions of the phases were determined by Rietveld refinement of XRD spectra. Scanning electron microscopy (SEM) in a XL30 Sirion FEG (FEI, Hillsboro, OR) was used to characterize the broader features of the microstructure and then to select specific locations to extract samples for transmission electron microscopy (TEM). Backscattered electron (BSE) and electron dispersive x-ray (EDX) detectors were used to identify two-phase regions suitable for TEM analysis. Electron probe microanalysis (EPMA) was used in some cases to complement the chemical analysis. TEM lamellae were extracted using a focused ion beam (FIB, Helios, FEI). Their microstructures were characterized in a Tecnai G2 Sphera TEM (FEI). High-resolution transmission electron microscopy (HRTEM), including high-angle annular dark field scanning TEM (HAADF-STEM, FEI Titan 300 kV FEG) was used to gain insight into the structures of the various phases present and the associated interfaces.

Thermal diffusivity was measured in Ar atmosphere between room temperature and 900 K using an Anter Flashline 3000 thermal flash apparatus (TA Instruments, New Castle, DE). Disk-shaped samples were prepared from the bulk using wire electrical discharge machining (EDM), 8 mm in diameter and 2 mm thick. After machining, the surfaces of the samples were ground and then coated by spraying with a carbon suspension to optimize absorption of the thermal pulse.

## Results

*Solidification Microstructure*.  The microstructure of the as-cast material provides the baseline for the study of the changes produced by the subsequent heat treatments.  The as-cast TiNi$_{1.2}$Sn comprises three phases identified by different contrast in Fig. 2(a): TiNi$_2$Sn (lighter grey), TiNiSn (medium gray), and Ti$_5$Sn$_3$ (darker grey), in addition to a small amount of Sn (white). EPMA traces across the main constituents in Fig. 2(a), avoiding the minor phases, revealed that the Ti:Sn ratio in all cases was essentially unity, with values ranging from 1.008 to 1.019 and standard deviations from 0.007 to 0.11.  The average composition of the fH dendritic regions was TiNi$_{1.72}$Sn and the hH interdendritic regions TiNi$_{1.11}$Sn.  The molar fractions of the phases were 41% (fH), 56% (hH), and 3% (Ti$_5$Sn$_3$).  These values are reasonably consistent with the relative area fractions of the fH (39%) and hH (50%) phases in Figure 2(a), as expected from their similar molar volumes.  The distinct dendritic shape of the fH regions clearly implies TiNi$_2$Sn is the primary phase formed during solidification, even though the overall composition is much closer to TiNiSn.  The behavior is consistent with the incongruent melting of the hH phase, as discussed elsewhere [21, 22].

*Lower temperature treatment*.  The as-cast material was given the initial heat treatment depicted in Fig. 1 (1173K/24h + 1123K/192K) for comparison with previous studies [21]. While it is recognized that the composition investigated should be two-phase at all temperatures below the solidus, this lower temperature (LT) treatment is designated as "homogenization" because it should remove much of the non-equilibrium segregation produced during solidification.  The resulting microstructure, Fig. 2(b), exhibits an increase in the proportion of hH (~77%) and a reduction in fH (~22%) compared with the cast material, as expected for the TiNi$_{1.2}$Sn composition.  Figure 3 shows there is also a significantly reduced fraction of Ti$_5$Sn$_3$ (~1%), consistent with is nature as a non-equilibrium segregate.  It is further noted in the latter figure that both the vestigial fH dendritic regions and the surrounding hH matrix contain sub-micrometer scale precipitates.  These observations were reported in an earlier study [21] and are further analyzed below using TEM, to gain insight on the nature, morphology, size distribution and orientation of the precipitates within each phase.

Observations on FIB lamellae extracted from the dendritic regions in Fig. 3 are shown in Fig. 4. EDX confirms that sub-micrometer, irregularly shaped hH precipitates are formed within the former fH dendrites.  The precipitates do not seem to exhibit any faceting indicative of crystallographic anisotropy, but do show a distinct cube-on-cube orientation relationship with the matrix, as inferred from the selected area diffraction pattern (SADP) in the inset of Fig. 4, collected at the interface between the two phases.  The SADP also reveals the splitting of diffraction spots away from the center, consistent with the 3% difference in lattice parameter (the

interior spot corresponds to the fH phase). The interface is semi-coherent, with clear evidence of misfit dislocations that accommodate the lattice mismatch, as seen in Fig. 4(b). These dislocations generate a region of local elastic strain that extends into the two phases and can, in principle, contribute to phonon scattering.

TEM analysis of a lamella extracted from the hH matrix in Fig. 3, depicted in Fig. 5, also reveals sub-micrometer precipitates, now corresponding to the fH phase, especially near the boundaries of the vestigial dendrites. These precipitates show the same cube-on-cube orientation relationship with the matrix as well as semi-coherent interfaces, although the shapes tend to be more regular than those in fig.4.

HRTEM provides further insight into the structural differences between the hH and fH phases and their interfaces, as illustrated in Fig. 6. The distinguishing feature is associated with the structural sites at (¾, ¾, ¾), which are filled by Ni in the fH phase (L2$_1$, $Fm\overline{3}m$), and vacant in the hH structure (C1$_b$, $F\overline{4}3m$). Rows of vacant sites are thus evident in the hH structure but not in the fH structure when both are imaged on the [110] zone axis, as shown by the comparison of Figs. 6(b) and (c). The superposed atomic arrangement sketches reveal the locations of the different atoms. The HRTEM image of the interface between hH and fH in Fig. 6(a) shows the degree of coherency, with misfit dislocations accommodating the lattice mismatch marked by the symbol —⁄. The extra half-planes in Fig. 6(a) are of the (002) type, spaced every 33 planes on the hH side in agreement with the 3% lattice mismatch.

*Higher Temperature Treatments*. The second set of treatments was designed to assess the mutual solubility close to the solidus and its effects on the subsequent precipitation processes. For the purposes of this discussion the process is labeled as a "solution" treatment, with two variants at different cooling rates. SEM micrographs of the resulting microstructures are displayed in Fig. 7; TEM images of lamellae taken from the marked locations in Fig. 7 are depicted in Fig. 8.

Compared with the material homogenized at lower temperature, both the slow cooled (HT-SC) and quenched (HT-Q) samples show reduced fractions of vestigial dendrites, slightly smaller in HT-Q, suggesting further dissolution of the fH phase into hH at the higher temperature. The composition of the phases after quenching is considered more representative of the high temperature equilibrium. For the regions identified as fH and hH in Figure 7(b) the compositions measured by EDS were TiNi$_{1.77}$Sn$_{1.09}$ and TiNi$_{1.16}$Sn$_{1.08}$, respectively, which are not substantially different from those measured by EPMA for the as-cast structure, described earlier.

Both phases contain precipitates of their counterparts, although those are less evident in the quenched material, Fig. 7(b), and to some extent within the vestigial dendrites of the slow cooled

sample, Fig. 7(a). The HT-SC sample does show clear evidence of extensive precipitation within the hH matrix even under the SEM. These are more clearly illustrated in the TEM images from the lamella extracted from the regions marked in Fig. 7(a), shown in Fig. 8. The area in Fig. 8(a) corresponds to the interface between a vestigial fH dendrite and the surrounding hH matrix. The fH phase on the left contains semicoherent hH precipitates on the order of 100-200 nm, barely visible in this image because of the contrast. Somewhat larger precipitates (100-500 nm) of fH within the neighboring hH matrix are clearly evident on the right side of Fig. 8(a). These precipitates have the expected cube-on-cube orientation relationship with the matrix and misfit dislocations at the interface. There is a region seemingly denuded of precipitations near the interface between the two larger regions, presumably corresponding to one of the precipitate-free patches in Fig. 7(a).

The lamella from the middle of the hH region marked in Fig. 7(a) reveals a higher density of fH precipitates, shown in Fig. 8(b). These are similarly oriented relative to the matrix, but often appear in approximately linear arrays and exhibit a wider variety of morphologies and sizes, some as long as 1 μm. Where these arrays are present they seem to align along the ⟨100⟩ directions of the hH matrix. The SADP in the inset, taken to include a precipitate and the surrounding matrix, reveals slightly elongated spots corresponding to nearly superposed reflections of the two phases, closer than those in Figure 4.

TEM analysis of the HT-Q microstructure using a lamella from the location marked in Fig. 7(b) is shown in Figs. 9 and 10. The diffraction analysis reveals no common orientation across the larger fH/hH interface. When viewed at high magnification by HAADF-STEM it is found that the high temperature fH phase has decomposed on cooling to form hH precipitates with square platelet shapes, ≤10 nm on edge and moderate aspect ratios, as shown in Fig. 9(a,b). These precipitates appear fully coherent with the matrix, as no separate reflections for the hH and fH phases are observed in the SADP, Fig. 9(c). In this instance the alignment of precipitates along the ⟨100⟩ directions of the fH matrix is well developed. The average precipitate spacing within these rows is ~19±5 nm. The apparent volume fraction of hH precipitates seems larger than might be expected from the rather modest solubility of TiSn (or alternatively Ni deficiency) in the fH phase, i.e. TiNi$_{1.77}$Sn v. TiNi$_2$Sn, which would yield ~20% hH assuming essentially equivalent molar volumes. The hH phase also shows extensive fH precipitation, as illustrated in Fig. 10, reflecting a significant solubility for Ni at high temperature. The SADP shows no evident peak splitting, suggesting the precipitates are also fully coherent with the matrix. However, the morphology is significantly different than that of hH precipitates in fH, cf. Fig. 9. The fH precipitates arguably exhibit thin platelet shapes with high aspect ratio and long dimensions ranging from 10-50 nm. The measured precipitate spacing normal to their long

dimension is ~38±5 nm. As in Fig. 9, the volume fraction appears somewhat higher than that estimated from the excess Ni in the hH phase, i.e. ~16%. The effect, however, may be the result of the coherency strains.

*Thermal Properties*. Figure 11 depicts the measurement of the thermal conductivities as a function of temperature for the samples resulting from the different heat treatments described above, as well as that of a stoichiometric TiNiSn (x=0). Both of the HT thermal treatments yield initially lower thermal conductivities for the TiNi$_{1.2}$Sn alloys relative to the sample homogenized at the lower temperature, cf. Fig. 1. There is a modest reduction for the HT-SC sample, ~20% relative to the LT (low temperature) sample, with the dependence of $\kappa$ on temperature during cooling being essentially the same as on heating. The reduction is substantially larger for the HT-Q material relative to that cooled slowly after the solution treatment, by as much as 50% at ambient relative to the homogenized sample. Notably, the benefit does not appear to be robust. Upon heating above 600 K, there is an accelerated increase in conductivity, eventually approaching that of the HT-SC material (~6.5 Wm$^{-1}$K$^{-1}$) at the maximum temperature. However, the behavior of $\kappa$ for the HT-Q material on cooling is essentially the same as that of the HT-SC sample. Further cycles exhibit essentially the same behavior on heating and cooling for both the HT treatments.

TEM analysis of the two major constituents of the HT-Q alloy after the thermal conductivity measurements to 873 K are presented in Fig. 12. No significant coarsening of the hH precipitates within the fH regions appears to have occurred, as inferred from comparing the precipitate spacings in Figs. 9(a) and 12(a), i.e. 19±5 nm and 21±5 nm, respectively. Some changes, however, seem to have occurred within the majority hH constituent, depicted in Fig. 12(b), where the fH precipitates appear to be more abundant with shorter average spacing normal to their long dimension (~11±2 nm) than prior to the measurement (38±5 nm), albeit not noticeably coarser than those in Fig. 10.

**Discussion**

*Phase Evolution during Solidification*: Understanding the phase and microstructure evolution during solidification requires a quantitative description of the liquidus and solidus surfaces in the Ni-Sn-Ti ternary, which has only recently become available [22]. The portion of the liquidus surface relevant to the present problem is depicted in Fig. 13(a). Understanding the solidification path is further facilitated by the fact that the Ti:Sn ratio remains very close to unity through the crystallization of both fH and hH phases, as noted earlier. These ratios are also maintained in the compositions of the constituents after the heat treatments. The inference is that much of the thermal history during solidification is contained in the schematic isopleth in Fig. 13(b), adapted

from [22].  The schematic is reasonably consistent with the reported congruent melting of the fH phase at 1720K and the incongruent melting of hH at ~1455K [21].

The fH dendrites in the as-solidified microstructure reveal this is the first phase forming from the melt ($C_0$), with the measured average composition marked on the fH solidus in Fig. 13(b).  As the fH phase crystallizes the melt is depleted only of Ni because of the solid and liquid have the same Ti:Sn=1 ratio.  Hence, the solidification path on the liquidus traces a line directly away from the TiNi$_2$Sn composition toward TiNiSn, as shown in Fig. 13(a). (Note in Fig. 13 that even a nominally stoichiometric hH phase would start solidification by forming fH dendrites.) According to the recent thermodynamic assessment the path should intersect the L+fH+Ti$_5$Sn$_3$ two-fold saturation line, whereupon the latter phase should form if there were no kinetic hindrance to its nucleation.  The microstructures in Figs. 2(a) and 3, however, show that the Ti$_5$Sn$_3$ phase forms later in the process.  Instead, the fH dendrites are surrounded by hH with a common orientation relationship and the same Ti:Sn=1 ratio, in a morphology reminiscent of a peritectic reaction in a binary system. Because of the close crystallographic relationship between the fH and hH phases it is hypothesized that nucleation of hH is more competitive than that of the unrelated Ti$_5$Sn$_3$.  Given the proximity of the liquid composition at the end of primary solidification to the invariant reaction L + fH + Ti$_5$Sn$_3$ → hH (P in Fig. 13a), if there were any kinetic delay in the nucleation of Ti$_5$Sn$_3$ the system would soon thereafter reach the L+fH+hH line, which would trigger the solidification of hH; that would continue on the same isopleth (Ti:Sn=1), directly away from the stoichiometric TiNiSn (hH) composition.[1]  This results in a range of Ni content in the hH phase, with an average denoted by the circle on top of the hH field in Fig. 13(b), supporting the view that solidification of hH proceeds for some time on the metastable extension of the hH liquidus surface.  However, at some point the depletion of Ni is sufficient to trigger the formation of the Ti$_5$Sn$_3$ phase, which appears in the last liquid pockets.  The solidification path would then turn away from the Ti:Sn=1 isopleth toward the Sn rich corner in Fig. 13(a), perhaps following, albeit briefly, the L+hH+Ti$_5$Sn$_3$ line.  The absence of Ti$_6$Sn$_5$ in the as-cast microstructure suggests solidification ends before the proposed L+Ti$_5$Sn$_3$ → hH + Ti$_6$Sn$_5$ reaction (U in Fig. 13b).  It is then suggested that the traces of Sn found in the as-cast structure may be the result of solid-state precipitation rather than segregation from the melt.

The amount of fH phase in the as-cast microstructure is clearly much higher than that expected at equilibrium in Fig. 13(b), as inferred from the substantial reduction in the area covered by the

---

[1]    There is some confusion in ref. [22] Gürth M, Grytsiv A, Vrestal J, Romaka VV, Giester G, Bauer E, et al. On the constitution and thermodynamic modelling of the system Ti–Ni–Sn. RSC Advances 2015;5:92270-91. about the nature of the reaction at the intersection of the fH, hH and Ti$_5$Sn$_3$ primary crystallization surfaces, but the microstructure is consistent with the scenario described in Fig. 13(a).  Note, however, that a true ternary peritectic reaction would involve 4 phases, not 3.

vestigial fH dendrites after the heat treatments. This is consistent with the diffusionally constrained completion of the "peritectic" reaction by surrounding of the fH dendrites with hH, which leaves excess fH phase. More importantly, the observation that both the dendritic (fH) and surrounding interdendritic (hH) constituents solidify with compositions over a range of Ni contents has important implications for the understanding of the phase equilibria and subsequent precipitation. The schematic range of fH phase compositions, marked by the thicker grey arrow on the fH solidus in Fig. 13(b), falls entirely within the fH+hH two-phase phase field at lower temperatures and thus precipitation of hH within fH would be expected in the as-solidified material. More importantly, the range of measured compositions for the hH regions, denoted again by a thicker grey arrow on the hH solidus in Fig. 13(b), would fall within the two-phase field. Hence, the solidus trace for hH must extend into the Ni-rich side of TiNiSn at the higher temperatures. The implication is that the hH phase may not melt incongruently at a single temperature, 1453K, as reported earlier [23], but is likely to involve multiple stages as suggested by Fig. 13(b).

*Precipitate Evolution*: It is instructive to discuss first the results from the higher temperature solution treatments, starting with the quenched condition (HT-Q). The microstructure consists of two major constituents, namely an hH matrix containing nanoscale fH precipitates, Fig. 10, and vestigial fH dendrites containing nanoscale hH precipitates, usually aligned in bands at orthogonal directions, Fig. 9. The precipitates are nominally coherent in both cases, exhibiting a cube-on-cube orientation relationship with their respective matrices and no evidence of peak splitting in the SADPs. The spacing of the mismatch dislocations identified in Fig. 6 compared with the dimension of the precipitates suggests that the hH precipitates in fH (Fig. 9) are fully coherent, whereas the fH precipitates in hH (Fig. 10) are semi-coherent along their habit plane.

SEM/EDS and EPMA measurements provide clear evidence that neither of these regions has the stoichiometry corresponding to the fully ordered compound at 1423K, i.e. the fH and hH phase are solid solutions respectively depleted and enriched in Ni while preserving the Ti:Sn=1 ratio, as shown in Fig. 13(b). The implication is that the deviations from stoichiometry are accommodated by fractional occupancy of Ni in the nominally empty sites for hH, or vacancies in the normally filled sites in fH [16, 24]. While the finite width homogeneity range for the fH phase has been discussed previously in the literature [25] much less is known about the solubility range for the hH phase, although prior reports of nanoscale precipitation of fH in hH would clearly imply such solubility [7, 17, 26].

The difference in morphology between the fH and hH precipitates in the HT-Q sample is arguably relevant to their role in the thermal conductivity, as discussed later, and intriguing because the matrix and precipitate phases are the same, with the same elastic mismatch but

different volume fractions and elastic properties. The formation of rows of hH platelets with a square base in Fig. 9(a) is reminiscent of the rows of cuboidal L1$_2$ precipitates in γ/γ' superalloys [27]. While both hH/fH and γ/γ' systems involve cubic precipitates in cubic matrices, the hH precipitates are not cubes but platelets thinner in one dimension and arranged in orthogonal directions, presumably to minimize the overall strain. This is even more evident in the dispersion of fH precipitates in hH, Fig. 10, which have a higher aspect ratio and no distinguishable alignment in rows.

A rigorous analysis of the precipitate shape evolution such as those undertaken for the γ/γ' superalloys, e.g. [27, 28], is well beyond the scope of this paper and likely to be hindered by inadequate information on relevant properties. Some insight, however, can be gained from the earlier analyses for the morphology of precipitates that included the effects of anisotropy, e.g. [29]. In essence, the simplified criterion for the preference for a plate/disk morphology over a sphere when the plate is oriented normal to a ⟨100⟩ direction is given by:

$$\frac{1}{2}\left(\frac{5}{2A+3}+\frac{2+3A}{5A}\right)C_{44} > \frac{C_{44}^*}{A^*} \tag{1}$$

where (*) denotes quantities for the precipitate and $A=2C_{44}/(C_{11}-C_{12})$ is the Zener anisotropy ratio [30] of the matrix or precipitate. The elastic constants calculated by DFT with the generalized gradient approximation (GGA) and including ionic relaxation [31] $C_{11}$, $C_{12}$ and $C_{44}$ are 172, 127 and 75, respectively, for the fH phase, and 196, 82 and 61, respectively, for the hH phase, respectively (all in GPa). Using these quantities for illustration, the anisotropy factors are $A^{fH}$=3.33 and $A^{hH}$=1.07. Inserting the proper values into Equation 1 the left hand side (matrix) is 46GPa for fH and 59GPa for hH, and the right hand side (precipitate) is 57GPa (hH) and 23GPa (fH). One can then show that the inequality is satisfied for fH precipitates in the hH matrix, but not for the reverse configuration. The latter, however, is more likely to be a cuboidal precipitate rather than spherical. More recent modeling on Ni alloys has shown that the aspect ratio of the precipitates would be larger (thinner) for the softer precipitate, which is the fH based on the $C_{44}$ values, consistent with the observations in Figs. 9 and 10. Note, however, that the arrangement of precipitates within the matrix can further modify the overall strain energy. The details remain to be elucidated by future investigations.

Slow cooling from the higher temperature solution treatment leads to similar combination of precipitates and matrices, but on a coarser scale, Figs. 7 and 8. The precipitates are more globular in shape, although many are still substantially elongated and some appear to have developed into more complex shapes within the hH regions, Fig. 8(b). In spite of the differences in morphology with those produced during quenching, the precipitates formed on slower cooling

also exhibit a clear cube-on-cube orientation relationship with the matrix but the SADP peaks are slightly elongated, suggesting partial loss of coherency. Figure 7(a) suggests the presence of a precipitate-free zone around the vestigial fH dendrites, also evident in the TEM image of Fig. 8(a) on the right side of the interface. This observation is consistent with the relief of the supersaturation of Ni within the hH phase by slight re-growth of the neighboring former fH dendrite rather than by nucleation within the hH phase.

Heat treatment at the lower temperatures should result in a lower volume fraction of precipitates within each of the larger fH and hH regions. It is likely, however, that these samples were not fully equilibrated during this treatment. The precipitates are globular and much larger in size than those resulting from the higher temperature treatment, still with cube-on-cube orientation relationships with their respective matrices but much less coherent, as shown by the extensive network of mismatch dislocations at the interfaces in Figs. 4 and 5. It is hypothesized that as the dendrites re-dissolve in the matrix to seek equilibrium their cores are the last regions to be affected. The precipitates already formed in these dendrite cores, either during cooling from solidification or at the early stages of the homogenization treatment, undergo coarsening as the outer boundaries of the dendrites recede. The same scenario is likely for the hH phase, which would experience coarsening of the fH precipitates formed earlier in the process. Hence, the vestigial fH dendrites and surrounding hH matrix exhibit some degree of inhomogeneity at the end of this treatment. The boundaries of the two-phase field have been ascribed on the basis of the average compositions, neglecting the inhomogeneity. Nevertheless, the results, at least for the fH regions, are consistent with those of Romaka et al. [25] at similar temperatures.

*Thermal transport properties*: It is known that microstructure, nanostructure, and point defects can all play a role in determining the thermal conductivity [32], given the spectrum of phonon mean free path lengths, and by extension *ZT*. Arguably the ideal microstructure would comprise a continuous, fine-grain polycrystalline hH matrix with discontinuous nanoscale intragranular precipitates of the fH phase and point defects, presumably in the form of excess Ni occupying the normally vacant (¾, ¾, ¾) interstitial sites. While the hH phase is not evidently continuous in the as-cast structure, dominated by the primary fH phase dendrites, Fig. 2(a), much of it has clearly become continuous after the LT homogenization treatment, Fig. 2(b), as expected from its composition and Fig. 13(b). Note, however, that a significant fraction of the overall hH phase content is present as isolated precipitates within the vestigial fH dendrites, Figs. 3 and 5. There are also fH precipitates within the hH matrix, but they are coarse and only partially coherent in spite of their common crystallographic orientation. More importantly, the residual fH dendrites are present in a sufficient proportion (~22%) to establish percolation paths. The net result of the fH phase content and distribution after the LT treatment is at best a modest effect in reducing κ

at ambient but no benefit at higher temperatures, as shown by the comparison of the LT samples for x=0 and x=0.2 in Fig. 11. The implication is that the rise in the electronic component of κ with increasing temperature, reported for the fH phase [21], and the percolation of the vestigial dendrites outweight any phonon scattering effects resulting from the presence of a second phase in the hH matrix.

After the HT-SC treatment there is a significant reduction in κ relative to the stoichiometric TiNiSn, at least at the lower temperatures in Fig. 11, with no significant penalty above ~650K. There is a significant reduction in the fraction of vestigial fH dendrites, as well as more extensive and uniform precipitation of fH within the hH matrix, Fig. 7(a), albeit only a modest reduction in the scale of the precipitates that remain only partially coherent. One may then ascribe the benefit primarily to the loss of connectivity of the vestigial fH dendrites. Neither the LT or HT-SC treatments shows any change in the dependence of κ on cooling, suggesting that the microstructures produced after the heat treatments are stable, even if the benefits are modest and limited to the lower temperatures.

The initially much larger reduction in κ resulting from quenching in Fig. 11, relative to the slow cooled sample cannot be related to the relative proportions of the coarser hH and fH constituents, which are the same as for the HT-SC. There is, however, a substantial reduction in the scale of the precipitates in both constituents. The hH precipitates are coherent and fully surrounded by the fH matrix, Fig. 9, in contrast with the somewhat larger, higher aspect ratio fH precipitates in hH, Fig. 10, which could arguably exhibit some connectivity. The implication is that the reduction in conductivity relative to the HT-SC sample could be ascribed to the finer scale of the fH precipitates, albeit mitigated by their connectivity. The absence of substantial coarsening after the measurement, Fig. 12, is inconsistent, however, with the higher conductivity measured upon cooling. The reduction in the spacing of the fH precipitates after the heat treatment suggests that the initial hH matrix was still supersaturated, leading to the additional precipitation during the heating step. One may then ifer that there was a significant contribution of the excess Ni remaining in the hH phase after quenching. This benefit is lost as the supersaturation is relieved, but while the number of fH/hH interfaces increases any benefit resulting from this change appears to be counteracted by the presumably increased connectivity of the fH platelets. The comparable conductivity after cooling between the present HT-Q sample and a composition with much lower Ni excess, namely TiNi$_{1.05}$Sn after the LT treatment [21], suggests some benefits of precipitate refinement may be feasible at lower Ni content, but one may also need to stabilize the point defects, perhaps by co-doping.

**Conclusions**

Bi-phasic hH/fH microstructures have been generated from a TiNi$_{1.2}$Sn alloy synthesized by levitation induction melting subjected to subsequent heat treatments. Extensive microstructural characterization and measurements of the thermal conductivity after different heat treatments led to the following conclusions.

All processing steps led to microstructures comprising coarse hH and fH constituents with precipitates of the counterpart phase in a scale depending of the heat treatment. The alloy should be nominally hH with a minor amount of fH as a second phase, but the solidification microstructure is dominated by the fH phase that forms first and is retained owing to the peritectic-like formation of hH which is diffusionally constrained from completion.

Upon heat treatment the hH phase becomes continuous but at lower temperatures the vestigial fH dendrites are still present in a volume fraction sufficiently high to form percolation paths that enhance the electronic component of the thermal conductivity counteracting any effect resulting from the presence of hH/fH interfaces. It is noted that even at the lower temperature treatment there is sufficient mutual solubility between the fH and hH phases to lead to the formation of precipitates within each constituent.

Solution treatment near the solidus increases the solubility range of both phases increases and the volume fraction of the corresponding precipitates on cooling. The fraction of vestigial fH dendrites is further reduced minimizing the percolation paths contributing to a desirable reduction in conductivity. The reduction is greater when the alloy is quenched from the high temperature, whereupon the precipitates in both of the major constituents are nano-scale. The scale of these precipitates tends to be sufficiently stable through the thermal cycle associated with the thermal conductivity measurement, but the initially large reduction in conductivity vanishes upon the cooling part of the cycle, becoming essentially identical to that for a sample with much coarser precipitates. The increase in the volume fraction of fH precipitates within the hH matrix suggests that the hH phase was supersaturated upon quenching, leading to excess Ni occupying the nominally vacant sites in the hH structure. Thus, the effects of the additional precipitation and associated increase in the fH/hH interfacial area appears to be counteracted by a loss of the point defect contributions to the thermal resistivity. These findings suggest possible paths to modify the microstructure by doping, adjusting the Ni content and tailoring the heat treatment to eliminate the coarser fH regions and retain a stable point-defect population to add to the effects of the fH/hH interfaces in phonon scattering.

**References**

1. Tritt TM. Thermoelectric Phenomena, Materials, and Applications. Annu Rev Mater Res 2011;41:433–48.

2. Zebarjadi M, Esfarjani K, Dresselhaus MS, Ren ZF, Chen G. Perspectives on thermoelectrics: from fundamentals to device applications. Energy Environ Sci 2011;5:5147-62.

3. Shakouri A. Recent Developments in Semiconductor Thermoelectric Physics and Materials. Annu Rev Mater Res 2011;41:399-431.

4. Yang J, Caillat T. Thermoelectric Materials for Space and Automotive Power Generation. MRS Bulletin 2006;31:224-9.

5. Bell LE. Cooling, Heating, Generating Power, and Recovering Waste Heat with Thermoelectric Systems. Science 2014;321:1457-61.

6. Rowe DM, Min G. Evaluation of thermoelectric modules for power generation. Journal of Power Sources 1998;73:193-8.

7. Xie W, Weidenkaff A, Tang X, Zhang Q, Poon J, Tritt TM. Recent Advances in Nanostructured Thermoelectric Half-Heusler Compounds. Nanomaterials 2012;2:379-412.

8. Uher C, Yang J, Hu S, Morelli DT, Meisner GP. Transport properties of pure and doped MNiSn „(M=Zr, Hf). Physical Review B 1999;59:8615-21.

9. Mastronardi K, Young D, Wang CC, Khalifah P, Cava RJ, Ramirez AP. Antimonides with the half-Heusler structure: New thermoelectric materials. Appl Phys Lett 1999;74:1415-7.

10. Hohl H, Ramirez AP, Kaefer W, Fess K, Thurner C, Kloc C, et al. A New Class of Materials with Promising Thermoelectric Properties: MNiSn (M = Ti, Zr, Hf). Mat Res Soc Symp Proc 1997;478:109-14.

11. Qiu P, Huang X, Chen X, Chen L. Enhanced thermoelectric performance by the combination of alloying and doping in TiCoSb-based half-Heusler compounds. J Appl Phys 2009;106:103703.

12. Sakurada S, Shutoh N. Effect of Ti substitution on the thermoelectric properties of (Zr,Hf)NiSn half-Heusler compounds. Appl Phys Lett 2005;86:082105.

13. Hohl H, Ramirez AP, Goldmann C, Ernst G, Wölfing B, Bucher E. Efficient dopants for ZrNiSn-based thermoelectric materials. J Phys: Condens Matter 1999;11:1697-709.

14. Dresselhaus MS, Chen G, Tang MY, Yang R, Lee H, Wang D, et al. New Directions for Low-Dimensional Thermoelectric Materials. Adv Mater 2007;19:1043-53.

15. Kimura Y, Tamura Y, Kita T. Thermoelectric properties of directionally solidified half-Heusler compound NbCoSn alloys. Appl Phys Lett 2008;92:012105.

16. Hazama H, Matsubara M, Asahi R, Takeuchi T. Improvement of thermoelectric properties for half-Heusler TiNiSn by interstitial Ni defects. J Appl Phys 2011;110:063710.

17. Makongo JPA, Misra DK, Zhou X, Pant A, Shabetai MR, Su X, et al. Simultaneous Large Enhancements in Thermopower and Electrical Conductivity of Bulk Nanostructured Half-Heusler Alloys. J Am Chem Soc 2011;133:18843–52.

18. Sootsman JR, Pcionek RJ, Kong H, Uher C, Kanatzidis MG. Strong Reduction of Thermal Conductivity in Nanostructured PbTe Prepared by Matrix Encapsulation. Chem Mater 2006;18:4993-5.

19. Kanatzidis MG. Nanostructured Thermoelectrics: The New Paradigm? Chem Mater 2010;22:648–59.

20. Faleev SV, Léonard F. Theory of enhancement of thermoelectric properties of materials with nanoinclusions. Physical Review B 2008;77:214304.

21. Douglas JE, Birkel CS, Verma N, Miller VM, Miao M-S, Stucky GD, et al. Phase stability and property evolution of biphasic Ti–Ni–Sn alloys for use in thermoelectric applications. J Appl Phys 2014;115:043720.

22. Gürth M, Grytsiv A, Vrestal J, Romaka VV, Giester G, Bauer E, et al. On the constitution and thermodynamic modelling of the system Ti–Ni–Sn. RSC Advances 2015;5:92270-91.

23. Jung D, Krosaki K, Kim C, Muta H, Yamanaka S. Thermal expansion and melting temperature of the half-Heusler compounds: MNiSn (M = Ti, Zr, Hf). Journal of Alloys and Compounds 2010;489:328-31.

24. Larson P, Mahanti SD, Kanatzidis MG. Structural stability of Ni-containing half-Heusler compounds. Physical Review B 2000;62:12754-62.

25. Romaka VV, P.Rogl, L.Romaka, Yu.Stadnyk, N.Melnychenko, A.Grytsiv, et al. Phase equilibria, formation, crystal and electronic structure of ternary compounds inTi–Ni–Sn and Ti–Ni–Sb ternary systems. Journal of Solid State Chemistry 2013;197:103–12.

26. Chai YW, Kimura Y. Microstructure evolution of nanoprecipitates in half-Heusler TiNiSn alloys. Acta Materialia 2013;61:6684–97.

27. Wang Y, Khachaturyan A. Microstructural evolution during the precipitation of ordered intermetallics in multiparticle coherent systems. Phylosophical Magarine A 1995;72:1161-71.

28. Voorhees PW, McFadden GB, Johnson WC. On the Morphological Development of Second-Phase Particles in Elastically-Stressed Solids. Acta Metallurgica et Materialia 1992;40:2979-92.

29. Schneck R, Rokhlin SI, Dariel MP. Criterion for Predicting the Morphology of Crystalline Cubic Precipitates in a Cubic Matrix. Metallurgical Transactions A 1985;16A:197-202.

30. Zener C. Contributions to the Theory of Beta-Phase Alloys. Physical Review 1947;71:846-51.

31. Hermet P, Niedziolka K, Jund P. A first-principles investigation of the thermodynamic and mechanical properties of Ni–Ti–Sn Heusler and half-Heusler materials. RSC Advances 2013;3:22176–84.

32. Zhao L-D, Dravid VP, Kanatzidis MG. The panoscopic approach to high performance thermoelectrics. Energy and Environmental Science 2014;7:251-68.
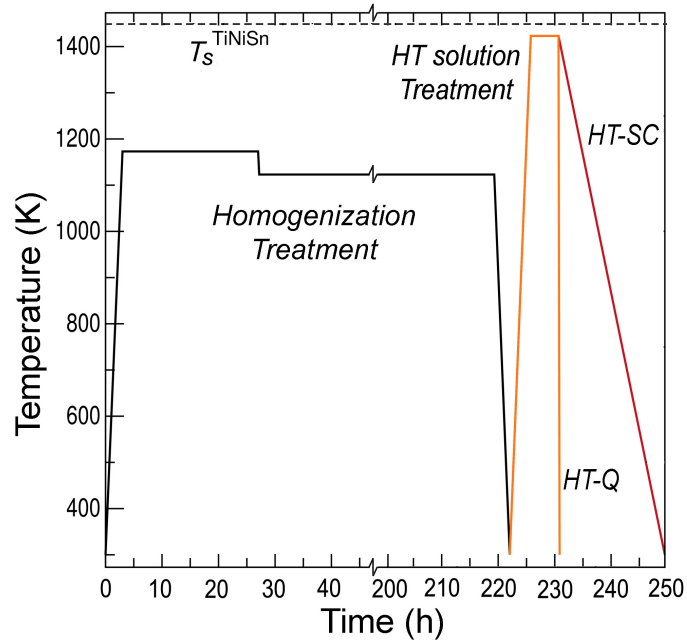
# Figures



Figure 1. Schematic showing the thermal history steps used to study the microstructure evolution in a TiNi$_{1.2}$Sn alloy. The solidus temperature of the half Heusler phase TiNiSn (~1450K) [22] is marked.
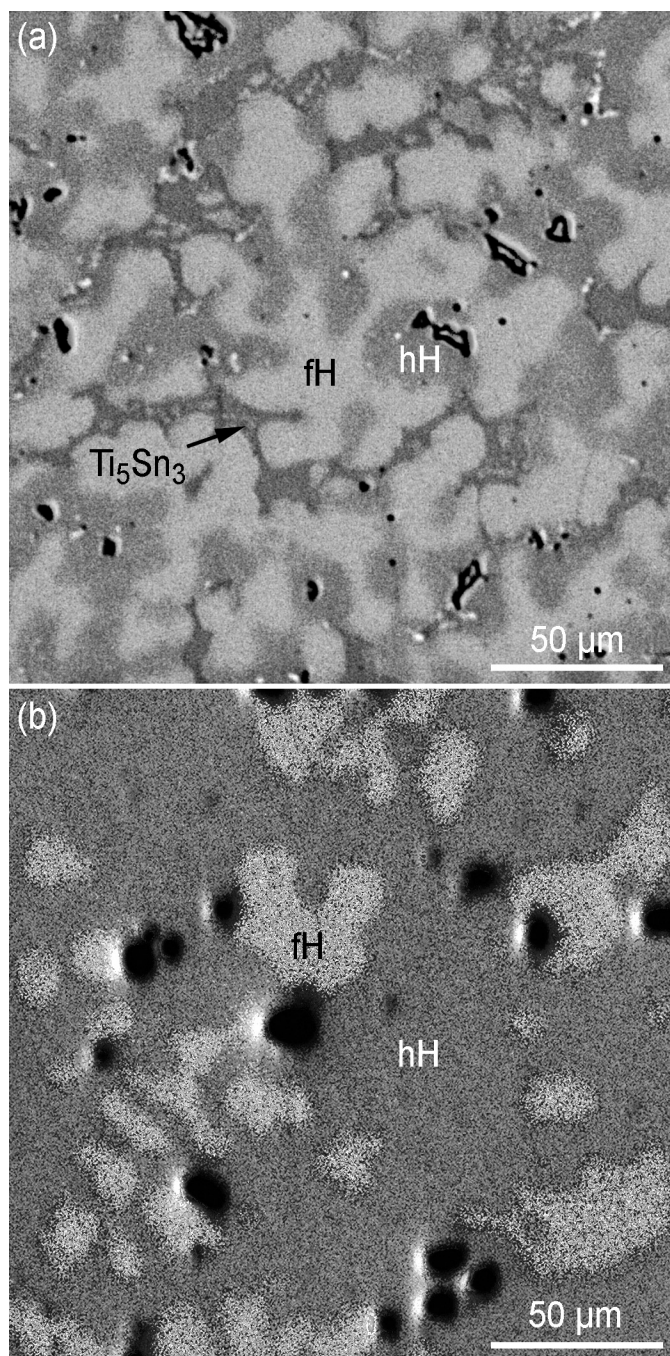
Figure 2.  Optical micrographs of the $TiNi_{1.2}Sn$ alloy in the (a) as cast condition and (b) after the homogenization treatment in Figure 1. The primary dendritic phase in (a) is the full Heusler phase (fH) which is followed by solidification of the hH phase, which eventually evolves in to the matrix in (b).
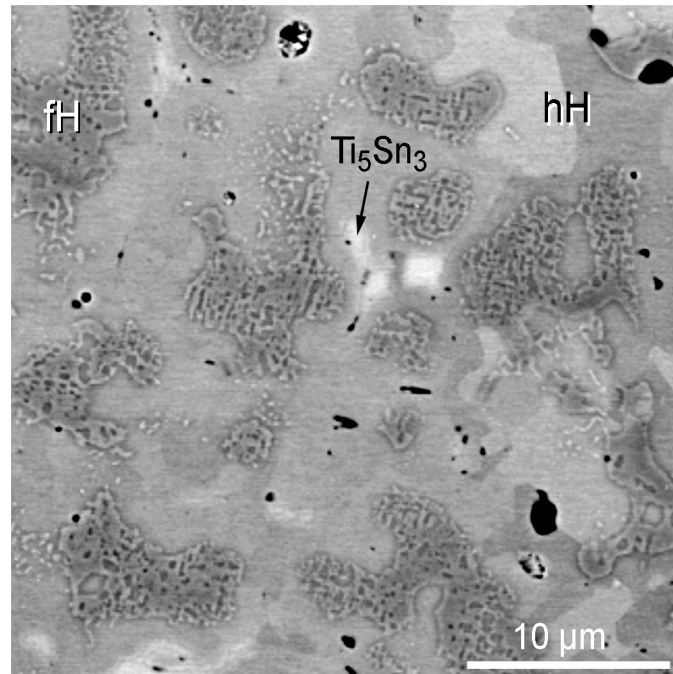
Figure 3. BSEI of microstructure for a TiNi$_{1.2}$Sn sample after the homogenization treatment. The lighest phase is residual Ti$_5$Sn$_3$, the much darker, mottled regions are the remnants of the fH dendrites, which have undergone some precipitation (cf. Fig. 4). The matrix is hH phase, which exhibits different intermediate levels of gray because of channeling contrast due to different orientations. A small amount of residual porosity appears as black features in the micrograph.
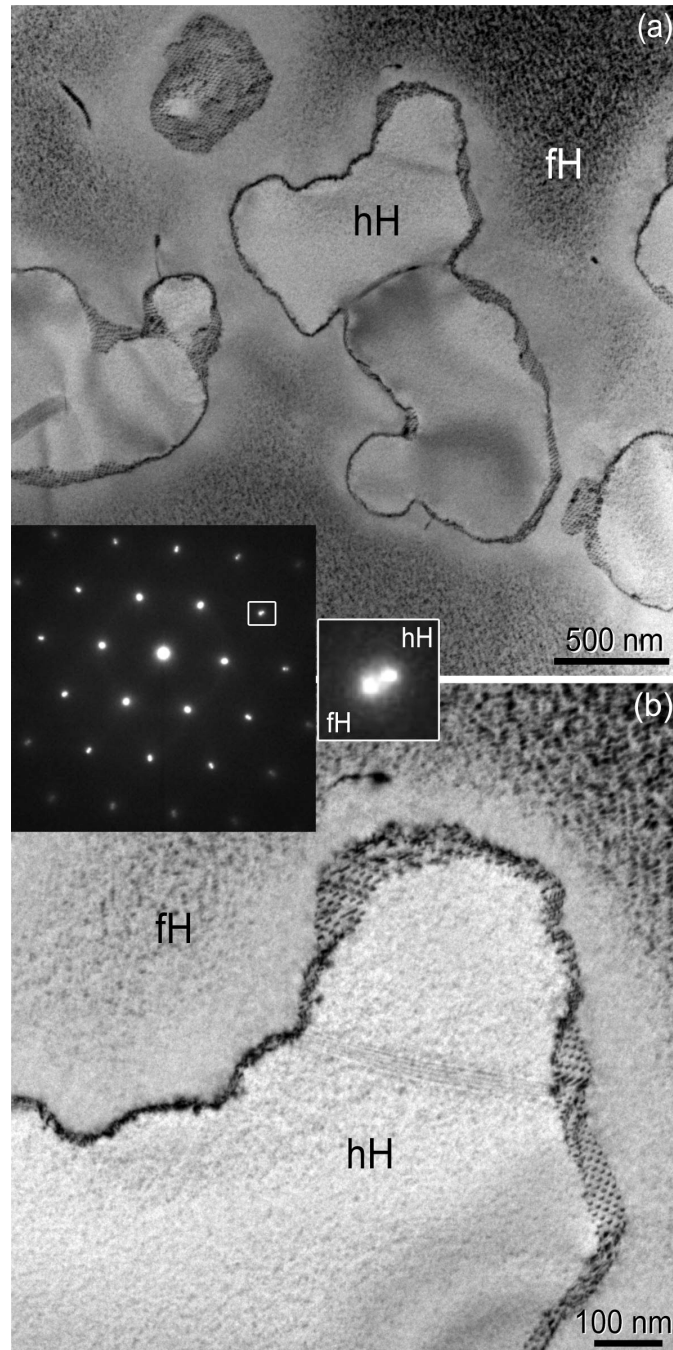
Figure 4. BF images of (a) hH precipitates within a former fH dendritic region, and (b) a close-up of the interfaces showing misfit dislocations. The [110] ZAP in the inset is from the interface between the fH and hH phases, with an enlargement of the spots marked by the small box showing the split between the fH and hH reflections due to the difference in lattice parameters.
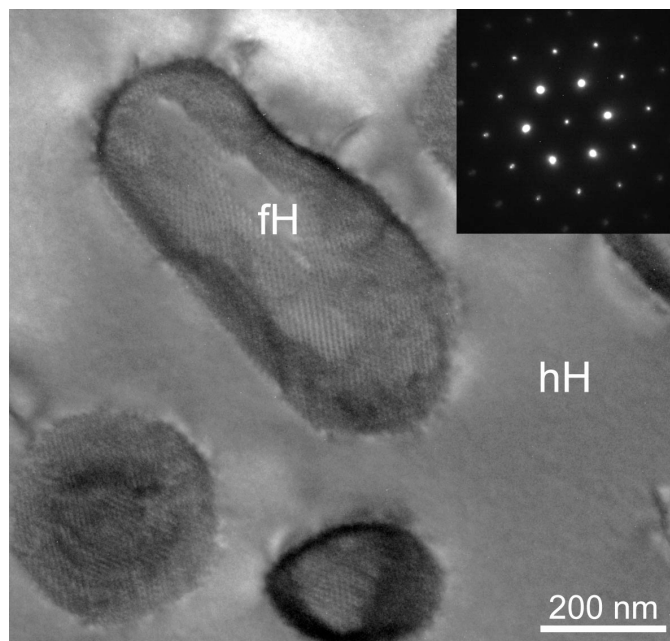
Figure 5. BF image of fH precipitates within the hH matrix surrounding the vestigial dendrites in Fig. 3. The [110] ZAP from the interface and surrounding phases shows the same orientation relationship between fH and hH as in Fig. 4, with similar splitting of the reflections.
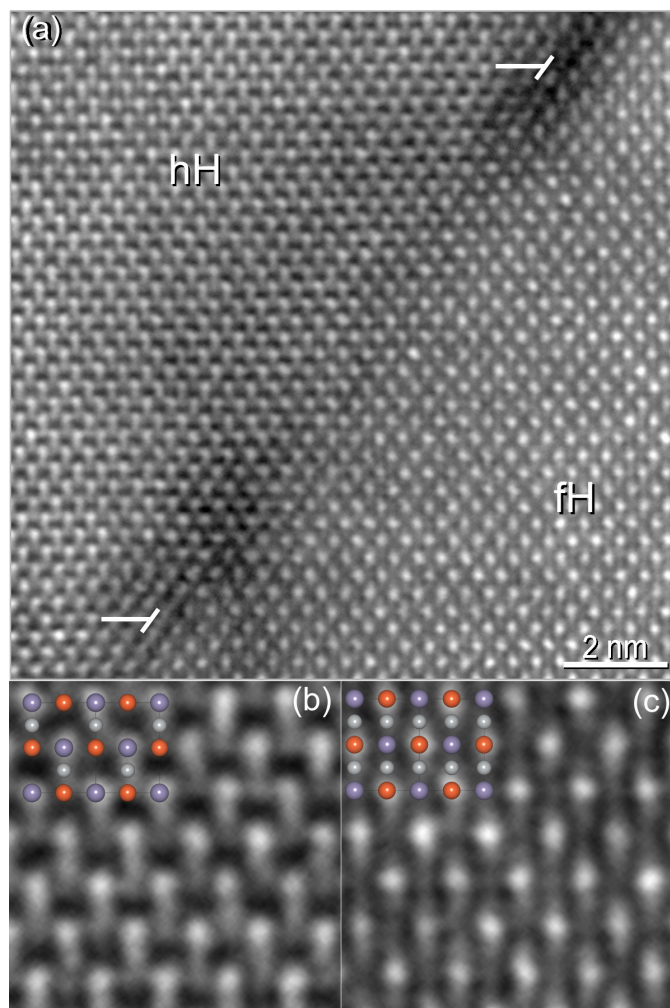
Figure 6. HAADF-HRTEM images of interface between fH and hH, with positions of misfit dislocations marked in (a). (b) shows an enlarged view of the hH phase overlaid with the atomic arrangement for the (110) plane, while (c) shows a similar arrangement for the fH phase.
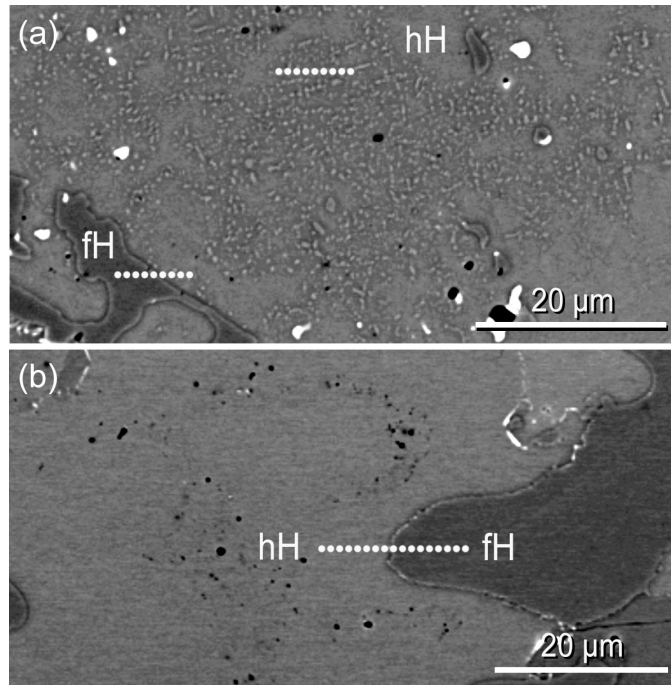
Figure 7. BSE images of the microstructures after the higher temperature solution treatment, (a) HT-SC and (b) HT-Q. The contrast between hH and fH in these images, where fH (TiNi$_2$Sn) appears darker than hH (TiNiSn), is thought to be due to the metallic nature of the fH, as the Z contrast is minimal between the two phases. The dotted lines indicate the positions from which TEM lamellae were extracted.
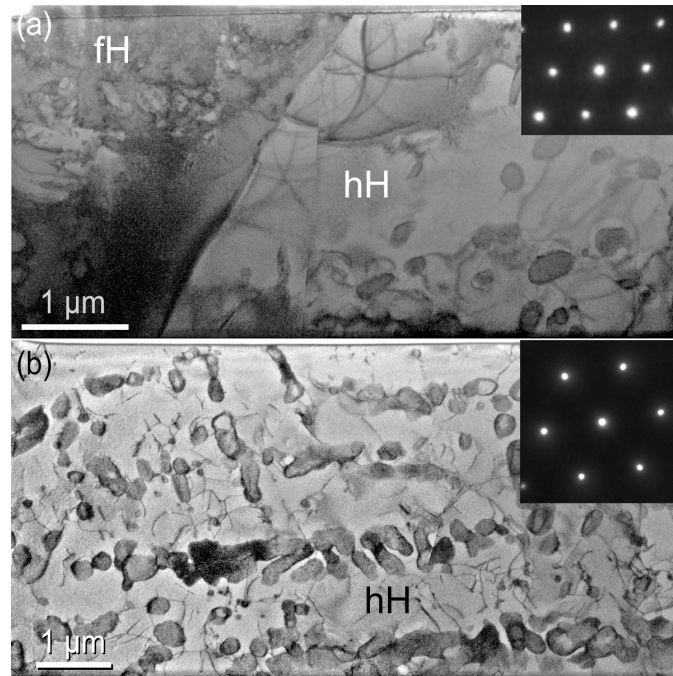
Figure 8. BF images of TEM lamellae extracted form regions marked in fig. 7(a) showing (a) the interfacial region between a vestigial fH dendrite and the surrounding hH matrix, and (b) the bulk of the hH matrix containing fH precipitates, often aligned in rows. The [110] ZAPs are from fH precipitates and the surrounding hH matrix in each case, showing the orientation relationship with closely spaced spots corresponding to each phase. The larger interface in (a) is incoherent.
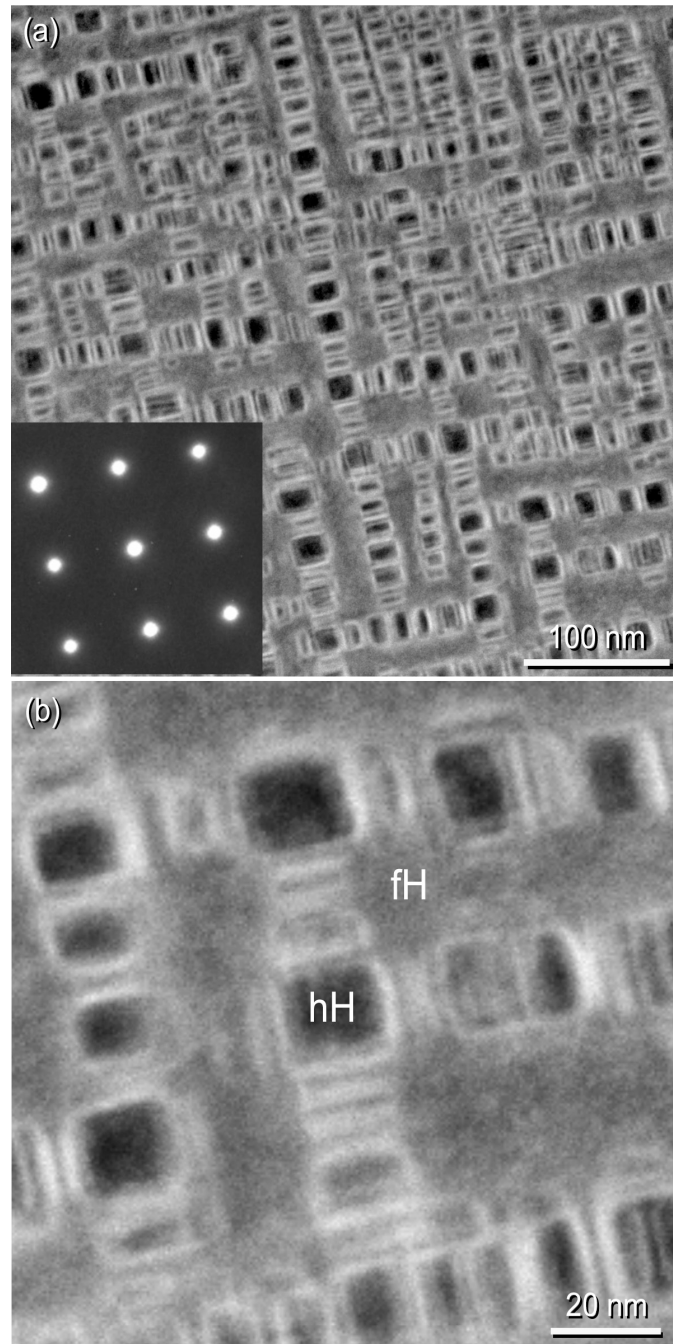
Figure 9. HAADF images of the region marked fH in Fig. 7(b) depicting ultrafine cuboidal hH precipitates within the fH vestigial dendrites. Note (a) the alignment of the precipitates along the ⟨100⟩ directions of the fH matrix, with (b) the sides of the precipitates aligned approximately in the same direction. The orientation relationship is confirmed by the [100] ZAP in the inset, which exhibits no evident splitting of the reflections that would be consistent with two distinct lattice parameters.
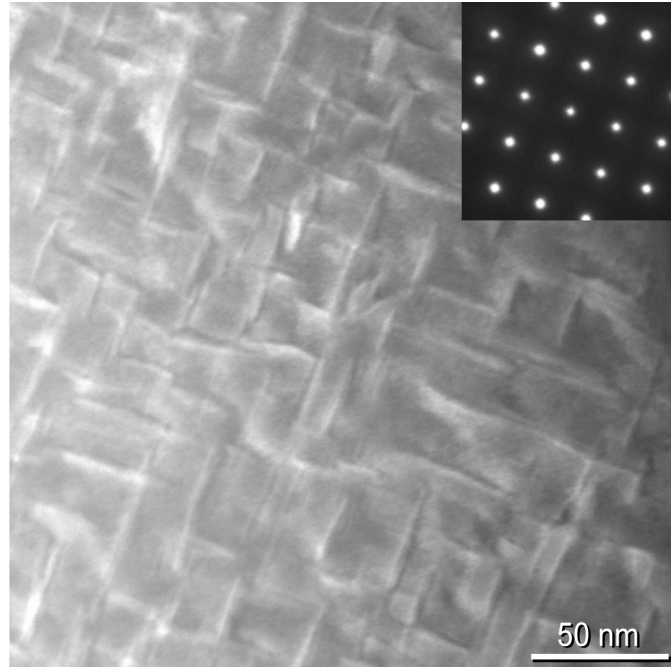
Figure 10. HAADF image of the region marked hH in Figure 7(b), showing high aspect ratio equiaxed platelets or disks of the fH phase within the hH matrix. The precipitates appear to be fully coherent. The [100] ZAP confirms the cube-on-cube orientation relationship but no distinct spots for the two phases..
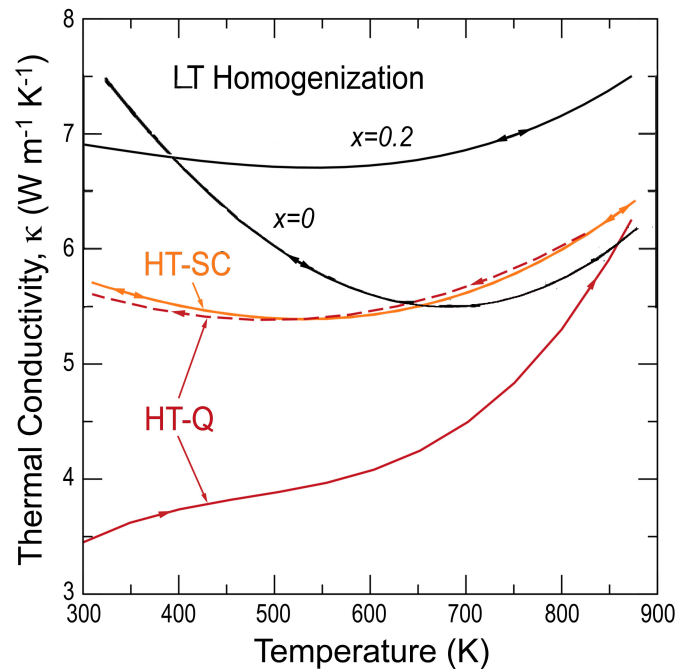


Figure 11. Thermal conductivity of TiNi$_{1.2}$Sn after the heat treatments defined in Fig. 1. All curves are for x=0.2 except the one marked as x=0. The dashed line corresponds to the measurements on the HT-Q specimen on cooling. Data for LT curves from reference [21].
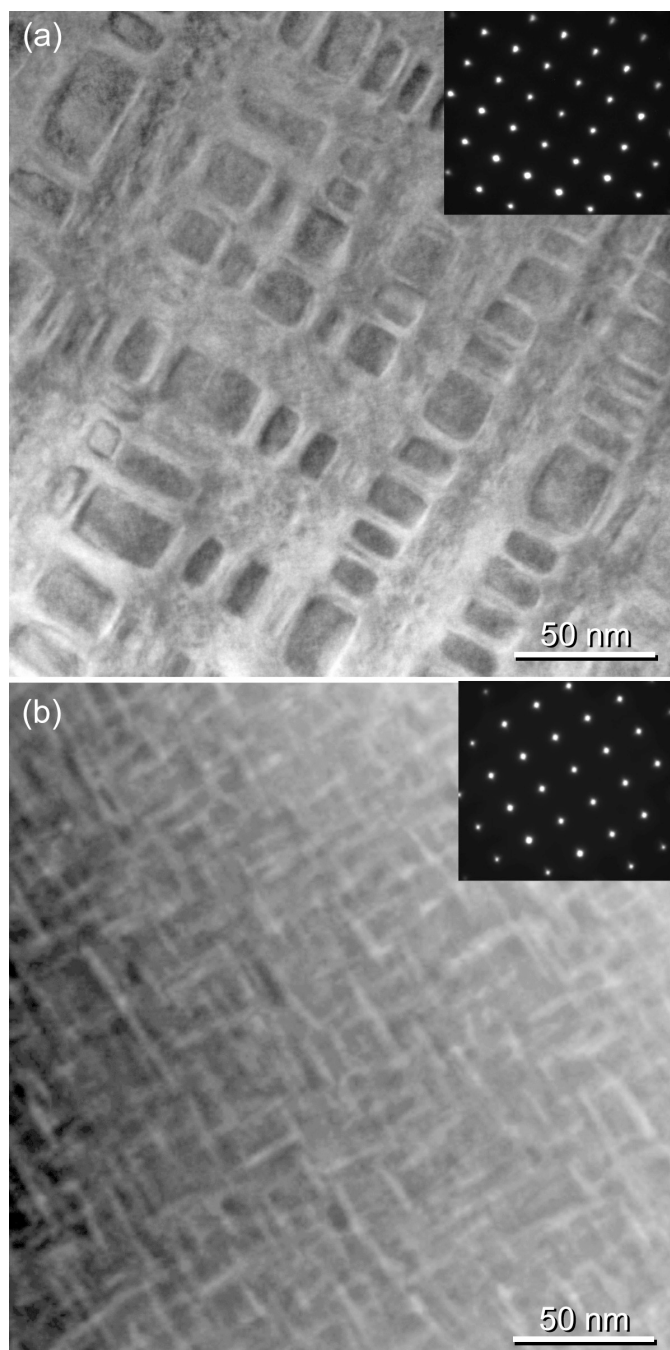
Figure 12. TEM images of the HT-Q specimen after the thermal conductivity measurements, wherein (a) is taken from a fH region with hH precipitates and (b) is from a hH region with fH precipitates. Compare the microstructures with their counterparts prior to the measurement in Figs. 9 and 10.
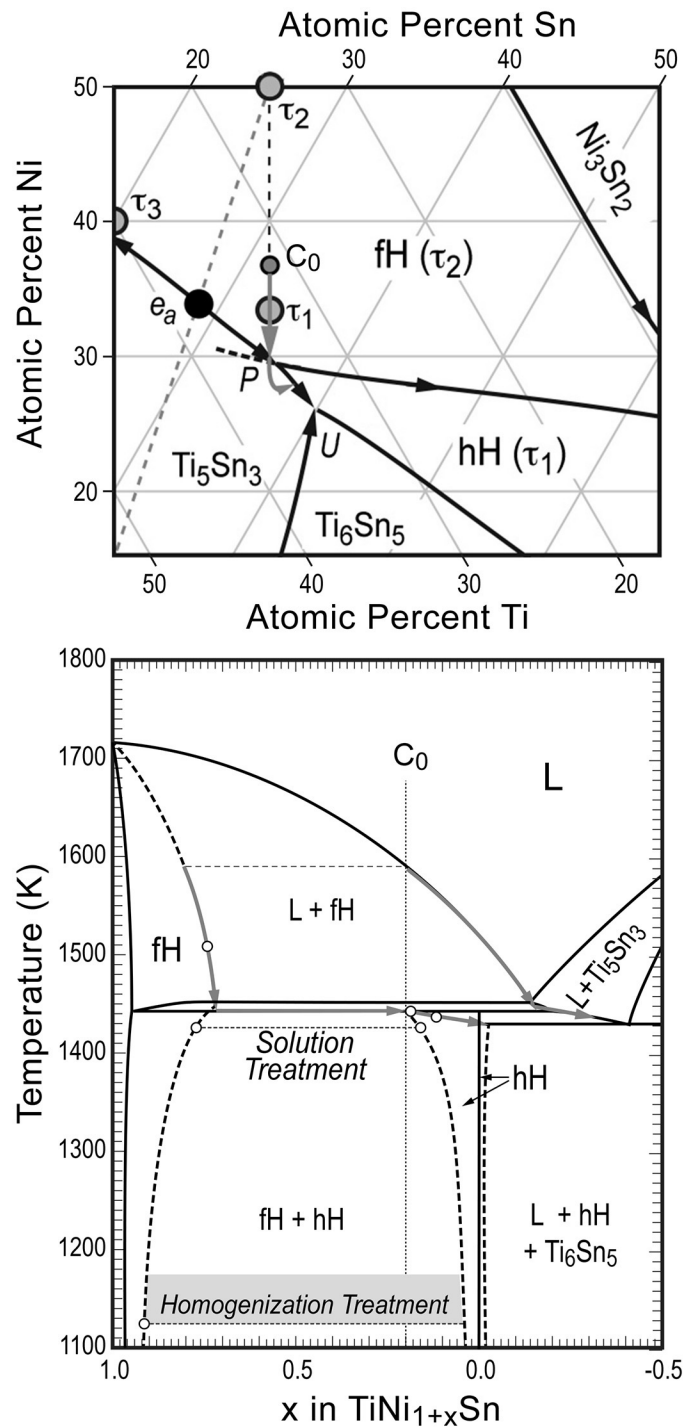
Figure 13.  Schematic of inferred solidification path along (a) the relevant portion of the Ni-Sn-Ti liquidus surface and (b) the isopleth with a constant Ti:Sn = 1 ratio, both adapted from [22].  The composition studied (x=0.2) starts solidification on the primary fH liquidus, with a higher average composition than expected from the calculated diagram.  Solidification continues with the formation of hH rather than Ti$_5$Sn$_3$ as proposed in the calculated diagram, which appears as the third phase due to non-equilibrium effects.  The solid compositions resulting from homogenization and higher temperature solution treatment are marked in (b).